2026 IEEE International Conference on Robotics and Automation (ICRA 2026)
June 1-5, 2026. Vienna, Austria

Closed-Loop Cross-Scale Motion of Decoupled Light- and Tendon- Driven Miniature Continuum Robots

Cheng Zhou, Xiaotong Qin, Haoyang Yu, Jingyuan Xia, Zheng Xu, Zecai Lin, and Anzhu Gao*

Abstract— **Small-scale robots are rapidly advancing in diverse fields such as industry and medicine. To be effective, they must be capable of accessing narrow, tortuous, or otherwise hard-to-reach environments and performing precise manipulation. This paper presents a vision-based closed-loop motion control scheme for a developed fiber-driven continuum robot for cross-scale motion. Function-multiplexed optical fibers are employed to achieve macro motion through fiber actuation and micro motion through light transmission within the fibers. An external eye-to-hand camera system observes a fiducial tag to estimate its 3D pose relative to the camera frame. The coordinate transformation between the tag and the end-effector is calibrated, along with the mapping between input laser power and light-induced joint contractions. A two-stage image-based visual servoing strategy is then implemented to guide the tag toward the target image position, thereby realizing closed-loop hybrid macro–micro motion through the developed kinematics and visual feedback. Point-tracking experiments demonstrate that the small-scale continuum robot, with an outer diameter of approximately 1.2 mm, can achieve precise cross-scale motion across workspaces ranging from tens of microns to the millimeter scale under the proposed control scheme. This work highlights the potential of hybrid macro–micro motion with visual servoing for deep access and high-precision operation in endoluminal interventions.**

I. Introduction

Miniaturized robotics are undergoing rapid development and playing an increasingly vital role across various research and industrial fields [1-6]. Their practical applications have expanded to include the high-precision assembly of small, complex products and the detailed inspection of industrial pipelines for search-and-rescue operations in inaccessible environments as well as for a wide array of diverse healthcare functions [7-11]. These operational settings are frequently characterized by confined, tortuous, or restricted geometries [12],[13]. There is a critical demand for small-scale robots that possess high positioning accuracy to ensure seamless and precise navigation within such complex spaces. [14-16].

To enable small-scale robots to adapt to confined environments, various small-scale robotics systems have been investigated [17-19]. Nwafor *et al.* designed a miniature 3-DoF glass fiber actuated parallel continuum robot. Each glass joint has an extension range from 6 to 15 mm and a diameter of 125 μm. And its capability, such as stiffness and manipulability were evaluated [20]. At the same time, they also present a new concept of a miniature concentric tube robot, which are widely used in medical applications. The proposed concentric tube robot is made of thermal treated capillary flexible concentric tube, the size of which is only 0.43 mm, and possess unprecedented radius of curvature that reaches as low as 5 mm. The demonstration, such as laser emission, fluid sample suction, and delivery operation, proved the robot have a good performance [21].

These miniature robots are typically endowed with macro-range motion with millimeter-scale accuracy [22-25]. Therefore, traditional miniaturized robots are often limited by the coarse positioning and maneuverability of instruments, making them difficult to perform micro and delicate tasks. To achieve high actuating accuracy, Suzuki *et al.* described an origami-inspired miniature manipulator with remote center of motion for teleoperated microsurgery. The results and features show that the mini robot has the potential in microsurgical procedures [26]. An *et al.* presented an image vision guided robotics system for automated brain electrode assembly under the microscope field-of-view, and the robotic system possessed submicron displacement accuracy for the precise control of the probe [27]. However, for practical robotic operation, it requires both rapid macro motion to reach to the target site and precise micro-motion for local manipulation, and thus needs a robot with cross-scale motion control. Hence, there is a need to design a robot capable of cross-scale manipulation, combining macro-level maneuverability with micro-scale precise positioning.

Existing approaches capable of cross-scale motion have been investigated [28-34]. A common method in minimally invasive robotic surgery is inserting the surgical instrument inside the patient's body for macro motion and a microsurgical robot are mounted on the tip of the instrument for micro operation. Vandebroek et al. proposed a concept of small-diameter multi-arm robot for intervention surgery. The design achieved an excellent decoupling of the macro platform and micro end-effectors [35]. Russo *et al.* designed a soft fluidic micro-actuator mounted on the top of an endoscope to realized cross-scale manipulation in a surgical scenario [36]. And to overcome the limitations of current robot architectures, and to enable image-based biopsy and micro-surgery in confined spaces, Giudice *et al.* achieved micro-motion through equilibrium modulation, which is realized by modulating the distribution of robots'

This work was supported in part by the National Natural Science Foundation of China (62422310, 62373248), the Science and Technology Commission of Shanghai Municipality (25ZR1402229, 25XF3201300), the China Postdoctoral Science Foundation (2025M771347), the Postdoctoral Fellowship Program of CPSF (GZC20250919). (Corresponding author: Anzhu Gao).

Cheng Zhou, Xiaotong Qin, Jingyuan Xia, Zheng Xu, Zecai Lin, and Anzhu Gao are with the School of Automation and Intelligent Sensing and Institute of Medical Robotics, Shanghai Jiao Tong University, Shanghai, China. Haoyang Yu is with the Institute of Medical Robotics, Shanghai Jiao Tong University, Shanghai, China.

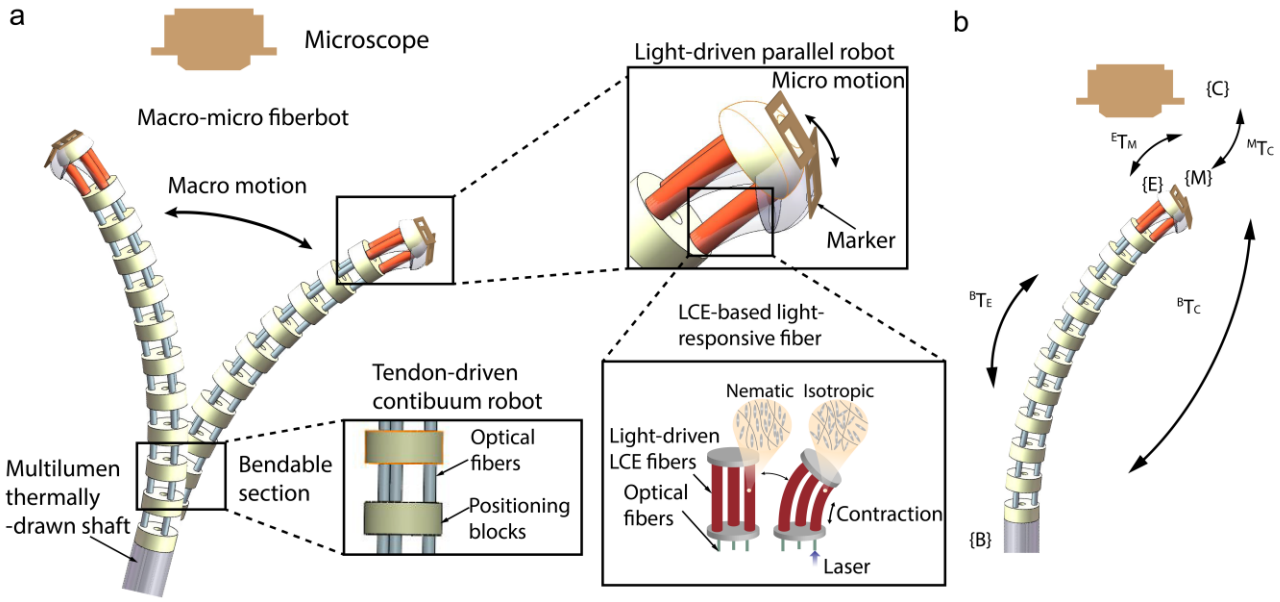

Figure 1. Schematic illustration of closed-loop control for cross-scale motion towards the miniature continuum robot. (a) The cross-scale miniature continuum robot comprises two main components: macro tendon-driven continuum robot and micro light-driven parallel robot. An ArUco tag is attached to the tip of the micro robot, and is relatively stationary with the end-effector. A camera is place above the tag to provide image feature recognition for closed-loop control. (b) Transformation matrix. Schematic of the coordinate frame transformations. {C}: camera frame; {M}: marker frame; {E}:end-effector frame of the robot; {B} base frame of the robot.

cross-sectional flexural rigidity of multi-backbone continuum robots [37]. To enhance the capability of macro robot, Lin et al. inserted a fiber with eccentric lumens into a continuum robot to produce micro-motion for a macro continuum robot. The results indicate that the repeatability of micro-motion is 10.1 μm [38]. Furthermore, to realize a higher positioning accuracy and bigger operation workspace, vision-based robotic system is utilized to improve control accuracy [39-41]. A robotic micromanipulation system enable precise and repeatable operations under a microscope was developed. The system utilized an external camera as macro visual feedback to obtain the macro field-of-view, to guide the tool into the microscope field-of-view. And then they used microscope to provide a micro visual servoing to implement micro-operation of the tool.

However, to realize cross-scale manipulation for intervention procedures, the associated challenges include miniaturized robot size, macro-micro trade-offs in terms of speed, range of motion and accuracy, and actuation cross-talk. Toward a small target in a confined space with tortuous access channels, possessing both high steerability and high positioning accuracy is necessary. Therefore, there has been a high demand for a small-scale continuum robot capable of cross-scale operation with high accuracy for targeted manipulation in a confined workplace. And vision-based feedback will help improve the cross-scale motion control accuracy.

The main contribution of this paper is the development of a vision-based closed-loop control scheme for a fiber-driven continuum robot capable of cross-scale motion. Function-multiplexed optical fibers enable macro motion via fiber actuation and micro motion via light-induced joint contraction. An external eye-to-hand camera tracks a fiducial tag to estimate its 3D pose, with coordinate transformation and laser power-joint mapping calibrated. A two-stage image-based visual servoing strategy guides the tag to the target, achieving closed-loop hybrid macro–micro motion through the developed kinematics and visual feedback. This work demonstrates the potential of hybrid macro–micro motion with visual servoing for deep access and high-precision operations in endoluminal interventions.

This paper is organized as follows. Section II describes the system design, including the macro–micro motion mechanism, the macro manipulator design, and the micro manipulator design. Section III presents the methodology, including the kinematic model of the macro–micro manipulator, image-based visual servoing control, the control strategy for macro–micro motion, and parameter calibration. Section IV introduces the experimental platform and validates the macro–micro motion using image-based visual servoing. Finally, Section V concludes this article.

II. Robot Design For Cross-Scale Motion

A. Cross-Scale Motion Mechanism

The proposed configuration of the fiber robot is shown in Figure 1(a). The intrinsically-decoupled optical fiber-actuated miniature fiber robot has a serial-parallel configuration, consisting of a macro tendon-driven continuum robot and a micro light-driven parallel robot. The same optical fibers are used for simultaneous mechanical and light actuations for both macro and micro motions. Here, three independent liquid crystal elastomer (LCE) fibers (outer diameter of about 300 μm) are assembled into a three degrees-of-freedom micro robot (outer diameter of about 1.2 mm), and three built-in optical fibers introduce light stimuli to the LCE fibers. Above that, a micro light driven parallel robot is mounted on the tip of

a macro robot. By controlling the output light intensity, precise motion can be achieved. The proposed concept with decoupled actuations lays the foundation for the macro-scale, rapid maneuvers and micro-scale, delicate operations toward endoluminal and endocavitary intervention.

B. Hardware System Design

Both macro robots and micro robots comprise three joints, which are arranged circumferentially at 120° intervals. The backbone of the macro robot is an elastic and straight nitinol wire arranged centrically with diameter of 200 μm. 3D printed spacer disks are rigidly attached to the nitinol backbone with equidistant spacing. Three optical fibers with over all diameter of about 250 μm are attach to the end disk of the robot to induce bending. Each optical fiber is routed in parallel to the nitinol backbone through holes of the spacer disks and multi-lumen shaft. Each optical fiber then is attached to a linear motor. The curvature of the macro continuum robot is controlled by linear motor actuation.

The structural design of the micro parallel robot is similar to that of the macro continuum robot described above. Both ends of each light-responsive LCE fiber are attached to two disks. Optical fibers are inserted into the LCE fibers to act as waveguides, delivering light to the LCE fiber matrix. The curvature of the macro continuum robot is controlled by the contraction of the LCE fibers.

An ArUco tag is attached to the tip of the micro robot and remains relatively fixed with respect to the end-effector. A high-resolution camera is placed above the tag to provide image-based feature recognition for closed-loop control.

III. Methods

A. Kinematics of Cross-Scale Motion

This section introduces the kinematic model of cross-scale motion. Constant curvature assumption is adopted for both macro and micro motion kinematic modeling due to their simplicity. To simplify the description, we take the micro robot as example to illustrate the kinematic model. The kinematics based on constant curvature can be decoupled into two parts. One is from the actuator space the to configuration space, and the other is from the configuration space to the task space. Here, the actuator space $\boldsymbol{q}$ consists of three actuator lengths q_1, q_2, q_3, while the configuration space consists of the bending plane angle φ, the bending angle θ, and arc length s. The task space here contains the position and orientation of the tip. The robot-specific mapping from LCE length (or optical fiber length) q_1, q_2 and q_3 to configuration space φ, θ, and s can be written as [42]

$$\varphi(\boldsymbol{q}) = \tan^{-1}\left(\frac{\sqrt{3}(q_2+q_3-2\cdot q_1)}{3(q_2-q_3)}\right) \tag{1}$$

$$\theta(\boldsymbol{q}) = \frac{2\sqrt{(q_1^{\,2}+q_2^{\,2}+q_3^{\,2}-q_1q_2-q_1q_3-q_2q_3)}}{3r} \tag{2}$$

$$\mathrm{s}(\boldsymbol{q}) = \frac{q_1+q_2+q_3}{3} \tag{3}$$

where r represents the distance from the center of the tendon to the center of the robot. From the configuration space to the task space, the homogeneous transformation matrix can be written as

$$\begin{aligned}
{}^{E}_{B}\boldsymbol{T} &= \begin{bmatrix} {}^{E}_{B}\boldsymbol{R} & {}^{E}_{B}\boldsymbol{P} \\ 0 & 1 \end{bmatrix} \\
&= \begin{bmatrix}
\cos^2\varphi\cdot(\cos\theta-1)+1 & \sin\varphi\cdot\cos\varphi\cdot(\cos\theta-1) \\
\sin\varphi\cdot\cos\varphi\cdot(\cos\theta-1) & \cos^2\varphi\cdot(1-\cos\theta)+\cos\theta \\
-\cos\varphi\cdot\sin\theta & -\sin\varphi\cdot\sin\theta \\
0 & 0
\end{bmatrix} \\
&\quad \begin{bmatrix}
\cos\varphi\cdot\sin\theta & s\cdot\cos\varphi\cdot(1-\cos\theta)/\theta \\
\sin\varphi\cdot\sin\theta & s\cdot\sin\varphi\cdot(1-\cos\theta)/\theta \\
\cos\theta & s\cdot\sin\theta\cdot/\theta \\
0 & 1
\end{bmatrix}
\end{aligned} \tag{4}$$

According to Eq. (1)-(4), the forward kinematics of continuum robot can be established. Then after derivation, the Jacobian matrixes from the actuating space to configuration space and from the configuration space to the task space can be calculated as shown in Eq. (5) and (6).

$$\begin{aligned}
\boldsymbol{J}_{a-c(3\times3)} &= \begin{bmatrix}
s\cdot\sin\varphi\cdot(\cos\theta-1)/\theta \\
-s\cdot\cos\varphi\cdot(\cos\theta-1)/\theta \\
0
\end{bmatrix} \\
&\quad \begin{bmatrix}
s\cdot\cos\varphi\cdot\sin\theta/\theta+(s\cdot\cos\varphi\cdot(\cos\theta-1))/\theta^2 \\
s\cdot\sin\varphi\cdot\sin\theta/\theta+(s\cdot\sin\varphi\cdot(\cos\theta-1))/\theta^2 \\
s\cdot\cos\theta/\theta-s\cdot\sin\theta/\theta^2
\end{bmatrix} \\
&\quad \begin{bmatrix}
-\cos\varphi\cdot(\cos\theta-1)/\theta \\
-\sin\varphi\cdot(\cos\theta-1)/\theta \\
\sin\theta/\theta
\end{bmatrix}
\end{aligned} \tag{5}$$

$$\begin{aligned}
&\boldsymbol{J}_{c-t(3\times3)} = \\
&\begin{bmatrix}
2\sqrt{3}(q_3-q_2)/(3(q_2-q_3)^2+(q_2-2q_1+q_3)^2) \\
-(q_2-2q_1+q_3)/(3r\cdot\sqrt{q_1^{\,2}+q_2^{\,2}+q_3^{\,2}-q_1q_2-q_1q_3-q_2q_3}) \\
1/3
\end{bmatrix} \\
&\quad \begin{bmatrix}
2\sqrt{3}(q_3-q_1)/(3(q_2-q_3)^2+(q_2-2q_1+q_3)^2) \\
-(q_1-2q_2+q_3)/(3r\cdot\sqrt{q_1^{\,2}+q_2^{\,2}+q_3^{\,2}-q_1q_2-q_1q_3-q_2q_3}) \\
1/3
\end{bmatrix} \\
&\quad \begin{bmatrix}
2\sqrt{3}(q_1-q_2)/(3(q_2-q_3)^2+(q_2-2q_1+q_3)^2) \\
-(q_1-2q_3+q_2)/(3r\cdot\sqrt{q_1^{\,2}+q_2^{\,2}+q_3^{\,2}-q_1q_2-q_1q_3-q_2q_3}) \\
1/3
\end{bmatrix}
\end{aligned} \tag{6}$$

Finally, the Jacobian from the actuating space to the task space with respect to the base coordinate frame can be calculate as

$$ {}^{B}\boldsymbol{J}_{E} = \boldsymbol{J}_{a-t} = \boldsymbol{J}_{a-c(3\times3)} \cdot \boldsymbol{J}_{c-t(3\times3)} \tag{7} $$

where ${}^{B}\boldsymbol{J}_{E}$ represent the Jacobian matrix from actuation space to the task space in base frame.

B. Image-Based Visual Servoing

This section describes the implementation of image-based visual servoing to verify the cross-scale capability of the miniature continuum robot. We consider an eye-to-hand robotic setup, where the camera is fixed and it coordinate frame defined as {C}, as shown in Figure 1(b). The robot end-effector defines frame{E}, and a fiducial tag (ArUco) rigidly attached to the end-effector defines frame {M}. A fixed camera observes the tag, which is rigidly attached to the miniature continuum robot's end-effector. The image-based visual servoing scheme for the cross-scale motion is illustrated in Figure 1(a). The goal of the image-based visual servoing is to actuate both the macro tendon-driven continuum robot joints and micro light-driven robot joints so as to minimize the image error $\boldsymbol{e}$ between the target points $\boldsymbol{p}^*$ and the observed robot features $\boldsymbol{p}$, using a set of image features in the image-plane coordinates

$$ \boldsymbol{e} = \boldsymbol{J}_{image}\dot{\boldsymbol{q}} \tag{8} $$

where $\boldsymbol{J}_{image}$ represents image Jacobian.

To facilitate easier and more accurate localization of the miniature continuum robot's end effector, a miniature ArUco tag is attached to the tip of the miniature continuum robot. The ArUco marker can detected by a high-resolution camera. After calibrating the camera's intrinsic parameters, the transformation from the camera coordinate {C} to the ArUco coordinate {M} can be calculated. Consequently, the position and orientation of the robot's end-effector relative to the camera coordinate can be determined.

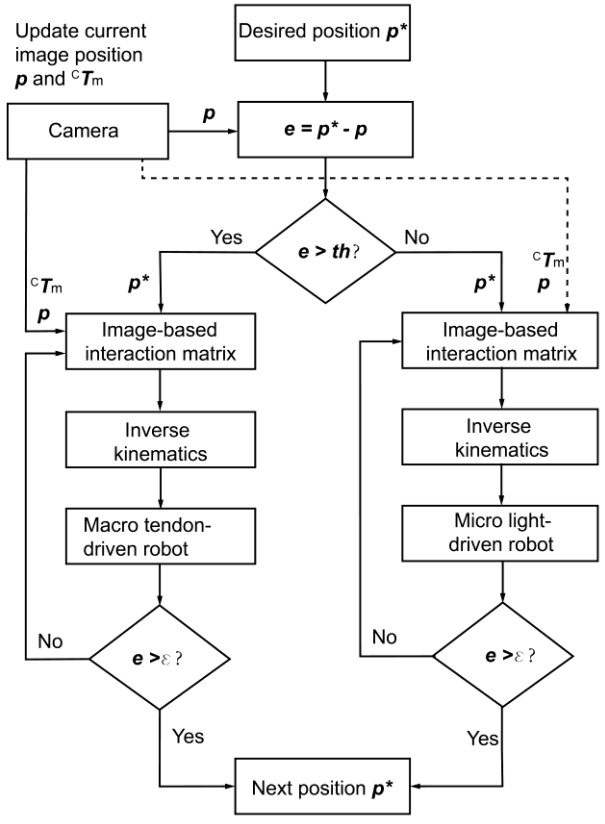

Figure 2. Schematic diagram for the control task flow. A two-stage image-based visual servoing strategy guides the tag to the target, achieving closed-loop hybrid macro-micro motion through the developed kinematics and visual feedback.

Before implementing image-based visual servoing procedure, the image Jacobian needs to be calculated. The image Jacobian is used to relate the spatial velocity of the marker to the time variation of the image features in the pixel plane. The spatial velocity of the marker can be expressed as

$$ {}^{C}\boldsymbol{v}_{M} = ({}^{C}v_{M}, {}^{C}w_{M}) $$

where ${}^{C}v_{M}$, ${}^{C}w_{M}$ denote the linear and angular velocities of the marker, respectively, and $\dot{\mathbf{s}}_{F}$ represents the time variation of the image features in the pixel plane.

Considering the eye-to-hand configuration, the relationship between $\dot{\boldsymbol{s}}_{F}$, and the object velocity ${}^{C}\boldsymbol{v}_{M}$ can be connected by an interaction matrix $\boldsymbol{L}_{M-F}$, which is given by

$$ \dot{\boldsymbol{s}}_{F} = \boldsymbol{L}_{M-F}\,{}^{C}\boldsymbol{v}_{M} \tag{9} $$

where the $\boldsymbol{L}_{M-F}$ can be descripted in terms of the spatial position of the marker in the camera frame, $\boldsymbol{X} = (X, Y, Z)$, and the position in the image plane, $\boldsymbol{x} = (x, y)$, projected from the spatial position. It then can be expressed as

$$ \boldsymbol{L}_{m-f} = \begin{bmatrix} -\frac{1}{Z} & 0 & \frac{x}{Z} & xy & -(1+x^2) & y \\ 0 & -\frac{1}{Z} & \frac{y}{Z} & 1+y^2 & -xy & -x \end{bmatrix} \tag{10} $$

To determine the projected position, the camera intrinsic parameters are used to map the spatial position of the marker onto the image plane

$$ x = \frac{X}{Z} = \frac{(u - \mathrm{u}_0)}{\mathrm{f}_x} \tag{11} $$

$$ y = \frac{Y}{Z} = \frac{(v - \mathrm{v}_0)}{\mathrm{f}_y} \tag{12} $$

where (u, v) denotes the real-time position of the image points expressed in the pixel coordinates, $\mathrm{u}_0, \mathrm{v}_0, \mathrm{f}_x, \mathrm{f}_y$ represent the camera intrinsic parameters.

By substituting ${}^{C}\boldsymbol{v}_{M}$ into (8), the relationship between the spatial velocity of the marker and actuated joints is established. The formulation can then be rewritten as

$$ {}^{C}\boldsymbol{v}_{M} = {}^{C}\boldsymbol{J}_{E}\dot{\boldsymbol{q}} = {}^{C}\boldsymbol{T}_{M}\,{}^{M}\mathbf{T}_{E}\,{}^{E}\boldsymbol{T}_{B}\,{}^{B}\boldsymbol{J}_{E}\dot{\boldsymbol{q}} \tag{13} $$

where ${}^{C}\boldsymbol{T}_{M}$, ${}^{M}\mathbf{T}_{E}$, ${}^{E}\boldsymbol{T}_{B}$ are the transformation matrix from marker frame to camera frame, end-effector to marker frame and end-effector to base frame, respectively.

$$ \dot{\boldsymbol{s}}_{F} = \boldsymbol{L}_{M-F}\,{}^{C}\boldsymbol{v}_{M} = \boldsymbol{L}_{M-F}\,{}^{C}\boldsymbol{T}_{M}\,{}^{M}\mathbf{T}_{E}\,{}^{E}\boldsymbol{T}_{B}\,{}^{B}\boldsymbol{J}_{E}\dot{\boldsymbol{q}} \tag{14} $$

Then time variation of the pixel feature can be replaced by pixel error, and to calculate the actuating length based on the image error, it can be denoted by

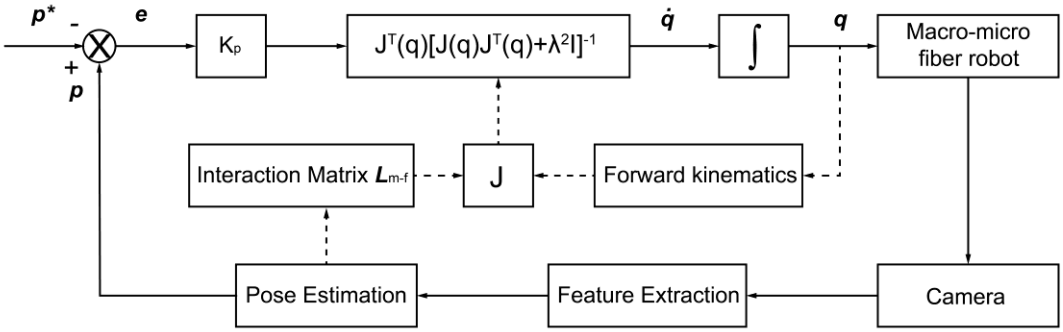

Figure 3. The closed-loop control diagram of the proposed image-based miniature continuum robot feedback control. The image Jacobian can be calculated with pose information and forward kinematics, and the image error will be eliminated through the feedback control.

$$\dot{\boldsymbol{q}} = \lambda \boldsymbol{J}_{image}^{+} \boldsymbol{e} = \lambda (\boldsymbol{L}_{M-F}\, {}^{C}\boldsymbol{T}_{M}\, {}^{M}\mathbf{T}_{E}\, {}^{E}\boldsymbol{T}_{B}\, {}^{B}\boldsymbol{J}_{E})^{+} \boldsymbol{e} \tag{15}$$

where $\boldsymbol{J}_{image}^{+}$ represents the pseudo-inverse of the image Jacobian and λ is a scale factor.

C. Calibration

In the eye-to-hand configuration, the camera is fixed above the robot to observe the end-effector. The vision system can directly provide measurements of the marker pose relative to the camera ${}^{C}\boldsymbol{T}_{M}$, where denotes the homogeneous transformation matrix of end-effector frame in the camera frame. And the transformation matrix ${}^{E}\boldsymbol{T}_{B}$ from robot base to end-effector can be calculated from robot's forward kinematics. So, we know that the only one unknown but constant transformation is the transformation between the end-effector and the marker, which is ${}^{M}\mathbf{T}_{E}$.

The marker pose and end-effector pose can be obtained from camera and forward kinematics, based on the constant equation

$${}^{C}\boldsymbol{T}_{M} = {}^{C}\boldsymbol{T}_{B}\, {}^{B}\boldsymbol{T}_{E}\, {}^{E}\mathbf{T}_{M} \tag{16}$$

we can know that the marker pose ${}^{C}\boldsymbol{T}_{M,i}$, ${}^{C}\boldsymbol{T}_{M,j}$ and end-effector pose ${}^{B}\boldsymbol{T}_{E,i}$, ${}^{B}\boldsymbol{T}_{E,j}$ can be obtained from camera and forward kinematics respectively, at any position and j in distinct frames. And the two equations can be rewritten as

$${}^{C}\boldsymbol{T}_{M,i} = {}^{C}\boldsymbol{T}_{B}\, {}^{B}\boldsymbol{T}_{E,i}\, {}^{E}\mathbf{T}_{M} \tag{17}$$

$${}^{C}\boldsymbol{T}_{M,j} = {}^{C}\boldsymbol{T}_{B}\, {}^{B}\boldsymbol{T}_{E,j}\, {}^{E}\mathbf{T}_{M} \tag{18}$$

we then take the inverse on both sides of equation (17) and substitute the result into equation (18), we can eliminate the unknown parameter ${}^{C}\boldsymbol{T}_{B}$, obtain

$${}^{E}\boldsymbol{T}_{M}\,({}^{C}\boldsymbol{T}_{M,i})^{-1}({}^{C}\boldsymbol{T}_{M,j})^{-1} = {}^{B}\boldsymbol{T}_{E,i}\, {}^{B}\boldsymbol{T}_{E,j}\, {}^{E}\mathbf{T}_{M} \tag{19}$$

Then a linear least-squares solution is used to solve the classic hand-eye calibration problem to figure out the transformation matrix ${}^{E}\mathbf{T}_{M}$.

For the micro light-driven parallel robot, the actuation is controlled indirectly through the input laser power $\boldsymbol{u}_p$, which induces light induced contraction via light-responsive mechanism. However, the kinematics control model requires the corresponding tendon length $\boldsymbol{q}$. Therefore, it is necessary to calibrate the functional mapping between the input laser power and the effective tendon contractions. A linear affine model of the form is developed as

$$\triangle \boldsymbol{q} = \mathbf{A}\boldsymbol{u}_p + \mathbf{b} \tag{20}$$

where $\boldsymbol{u}_p = [u_{p1}, u_{p2}, u_{p3}]$; $\triangle \boldsymbol{q} = [\triangle q_1, \triangle q_3, \triangle q_3]$; $\mathbf{A} \in R^{3\times 3}$ and $\mathbf{b} \in R^{3}$ are unknow calibration parameters.

Thus, the Jacobian from the actuation space to the input power space can be derived as follows

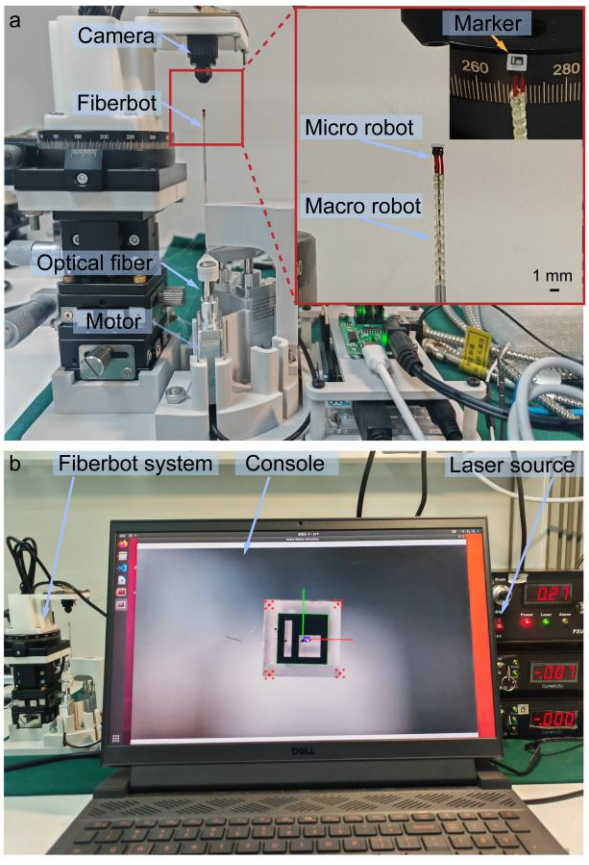

Figure 4. Setup of decouple light- and tendon- driven miniature fiber-shape continuum robots for macro-micro motion. An ArUco marker with an accuracy of 1 μm is attached on the end-effector of the fiberbot. A high-resolution camera is utilized to capture the image of the robot to facilitate image-based visual servoing control.

$$\dot{\boldsymbol{q}} = \mathbf{A}\dot{\boldsymbol{u}}_p \tag{21}$$

To calibrate the matrix, then the effective tendon is substitute into forward kinematics to obtain the transformation matrix ${}^{B}\boldsymbol{T}_{E}$, and the predicted ${}^{C}\boldsymbol{T}_{M,predict}$ is obtained

$${}^{C}\boldsymbol{T}_{M,predict} = {}^{C}\boldsymbol{T}_{B}\,{}^{B}\boldsymbol{T}_{E}\,{}^{E}\mathbf{T}_{M} \tag{22}$$

these parameters are optimized with the following objective function

$$\min \sum \left({}^{C}\boldsymbol{T}_{M,predict} - {}^{C}\boldsymbol{T}_{M,observe}\right)^{2} \tag{23}$$

After data acquisition and optimization, the mapping matrix from laser power input to light-induced contraction can be obtained.

D. Control Strategy for Cross-Scale Motion

As shown in the Figure 2, the schematic diagram depicts the control task flow of cross-scale motion control of the miniature continuum robot. The camera first gets the desired image position $\mathbf{P}^*$, and then selects an appropriate approach control strategy based on the initial image pixel error $\mathbf{e}$ between the target point and the current point $\mathbf{P}$. If the image error is greater than threshold th , macro actuation is executed; if the error is less than threshold th , micro actuation is triggered. Due to the independent macro and micro control, this strategy is implemented only at the initial stage of each movement.

The control logic of macro robot and micro robot is similar; herein, micro robot control flow is selected for later analysis. By incorporating the camera intrinsic parameters and robot's forward kinematics, the pose of the ArUco tag relative to the camera is derived from the image, followed by the computation of the image Jacobian matrix. Following the pseudo-inverse solution, the desired robot joint parameters are obtained. These joint parameters are then mapped to the laser power input values by Eq. (21) and rounded to integers, yielding the actual laser power input parameters. Subsequently, the actual robot joint parameters are updated simultaneously, thereby completing a single-step motion iteration. The control block diagram and control task workflow are shown in Figure 2 and 3.

IV. Experiments and Results

This section describes the setup of the experimental platform, camera intrinsic parameter calibration, and

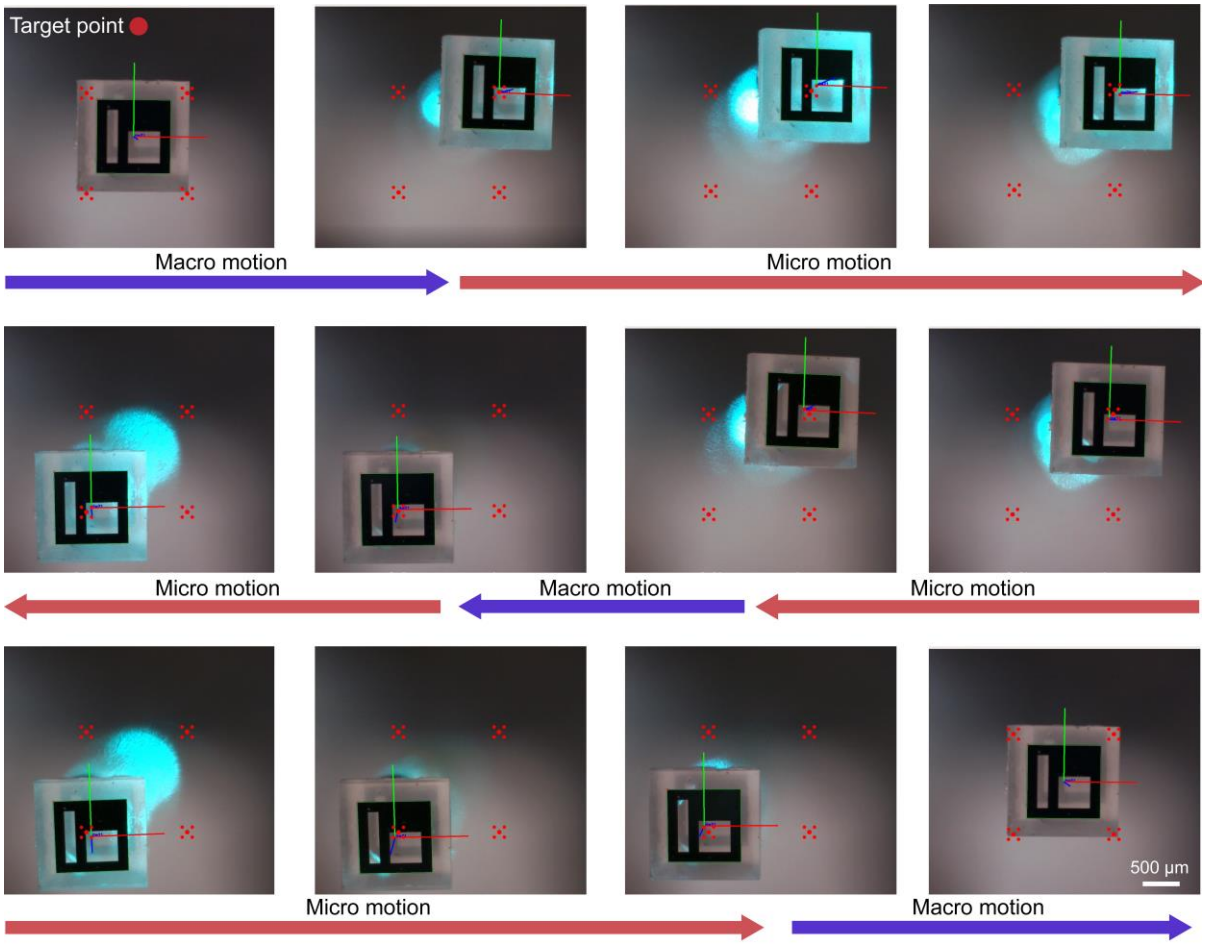

Figure 5. Demonstration of closed-loop control of cross-scale motion of the miniature continuum robot based on image-based visual servoing. The cross-scale miniature continuum robot was actuated to the first target point set in the middle point of the point cluster in the upper right corner through macro actuator. Then, the miniature continuum robot was guided to traverse the remaining four points within the point cluster located in the upper-right corner. And then, following this procedure, the miniature continuum robot completed the traversal of the remaining three point clusters.

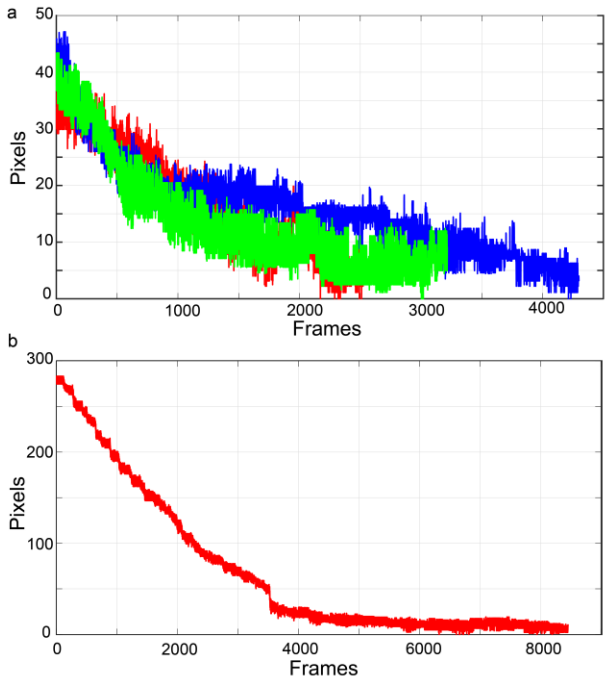

Figure 6. Results of the image distance between target points and initial image point. The data indicates that the system can converge to the target position in both micro (a) and macro (b) control.

closed-loop control results with eye-to-hand image-based visual servoing. Then, we analysis the results and present the captures and video of closed-control performance.

A. Experimental Platform

The experimental platform is shown in Figure 4. All positioning blocks in macro robot were fabricated by micro 3D printed technology (microArch S240, BMF Material Technology Inc., Shenzhen, China), assembled into the central backbone of the main body, and fixed using adhesive (Loctite 4013, Henkel, CT). And the bending segment was connected with a three-lumen thermally drawn polycarbonate. A total length of the macro continuum robot is 14 mm. Three linear motors (LASF16-024D, Inspire Robots. China) were used to actuate optical fiber tendons (Wuhan FiberHome International Technologies Co., Ltd. China). The light-driven fiber was fabricated follow the procedure in previous work [32]. Three laser power sources (Changchun New Industries Optoelectronics Technology Co., Ltd.; Lasever Inc. China) were used for micro robot joints actuation. A camera (HXY-317-35B) was mounted above the miniature continuum robot stationary to observe the ArUco tag. A 13×12 checkerboard (0.15×0.15 mm) was used to calibrate the intrinsic parameters of the camera based on classical Zhang's camera calibration algorithm. The resolution for calibration and image servoing process is 1920×1080. But the image shown in the computer was resized to show full frame. The transformation matrix from the camera to the tag could be calculated through opencv's code repository. All those for the macro and micro modules are performed by the corresponding ROS node.

B. Cross-Scale Motion Validation Based on Image-Based Visual Servoing

To validate the closed-loop control capability of our cross-scale control system, first we calibrate the two matrixes mentioned above. We initially actuated the macro robot to collect data along various directions, and subsequently calibrate transformation matrix ${}^{m}\mathbf{T}_{e}$ using a hand-eye calibration method. Subsequently, we actuated the micro robot under different laser power inputs and got the mapping matrix $\mathbf{A}$ from power to joint contraction by integrating kinematic models into the established calibration methodology.

As shown in Figure 5, it demonstrates closed-loop control of cross-scale motion of the miniature continuum robot based on image-based visual servoing. Four point clusters marked in red can be found in the figure. Four main image points were set for macro motion, at the same time, another four target satellite image points were set around each of the main point for micro motion. Follow the strategy described in Section III., we first selected an appropriate approach based on the initial image pixel distance between the target point and the current point. And then we carry out the following motion control. The cross-scale motion was actuated to the first main point set in the middle point of the point cluster through macro actuator. After that, the miniature continuum robot was guided to traverse the remaining four satellite points within the point cluster. And then, repeating this procedure, the miniature continuum robot completed the traversal of the remaining three-point clusters. Pixel error results in Figure 6. indicate that the robot can be controlled to rapidly converge to the target positions, thereby achieving precisely closed-loop control.

V. Conclusion And Future Work

This work demonstrates the actuation of a miniature continuum robot toward target coordinates via an image-based visual servoing framework. The control strategy adaptively selects the optimal motion trajectory based on the pixel distance in the image plane, thereby ensuring efficient navigation to the destination. This superior low cross-talk performance is attributed not only to the dual-stage closed-loop precision but also to the negligible intrinsic decoupled actuating mechanism. Such a decoupled control architecture ensures that micro-scale refinements and macro-scale movements can coexist without mutual interference, significantly enhancing the system's operational reliability.

While this study demonstrates independent cross-scale closed-loop motion, coordinated macro-micro manipulation coupled with robust control architectures could be implemented to facilitate the rapid tracking of complex trajectories [43]. As the current work represents a preliminary proof-of-concept, the reliance on an overhead camera and external fiducial markers may limit its immediate clinical translation. To facilitate real-world clinical deployment (e.g., within the ear canal), future iterations could integrate side-mounted, customized markers and front-view cameras into a unified, biocompatible interventional instrument.

Furthermore, data-driven strategies, such as model-free deep reinforcement learning, could be leveraged to address inherent challenges in classical visual servoing, particularly within highly constrained and unstructured environments [44]. We expect that this integrated, safety-aware framework will bridge the gap between laboratory prototypes and practical surgical tools, holding significant promise for advancing autonomous precision surgery in future clinical applications.

REFERENCES

[1] R. Bogue, *et al.*, "Miniature and microrobots: A review of recent developments," *Ind. Robot: Int. J.*, vol. 42, no. 2, pp. 98-102, 2015.

[2] L. Hines, *et al.*, "Soft actuators for small-scale robotics," *Adv. Mater.*, vol. 29, no. 13, 1603483, 2017.

[3] Z. Lin, *et al.,* "Progress in deformation sensing for flexible robots, " *Proc. IEEE,* vol. 113, no. 8, pp. 752-782, 2025.

[4] Z. Chen, *et al.,* "Bioinspired and biohybrid soft robots: Principles and emerging technologies," *Matter*, vol. 8, no. 4, 2025.

[5] C. Zhou, *et al.,* "Progress in probe-based sensing techniques for in vivo diagnosis, " *Biosens.,* vol. 12, no. 11, 943, 2022.

[6] J. Kahrs, *et al.*, "Continuum robots for medical applications: A survey," *IEEE Trans. Robot.,* vol. 31, no. 6, pp. 1261-1280, 2015.

[7] H. Gao, *et al.,* "Multi-axis robotic forceps with decoupled pneumatic actuation and force sensing for cochlear implantation, " *Nat. Commun.,* vol. 16, no. 1, 1648, 2025.

[8] A. Gao, *et al.,* "Spiral FBG sensors-based contact detection for confocal laser endomicroscopy, " *Biosens. Bioelectron.* vol. 170, 112653, 2020.

[9] C. Tang, *et al.*, "A pipeline inspection robot for navigating tubular environments in the sub-centimeter scale," *Sci. Robot.*, vol. 7, no. 66, eabm8597, 2022.

[10] Z. Xu, *et al.,* "Distributed proximity sensors-integrated hyper-redundant robots with augmented spatial shape for unstructured environment exploration, " *IEEE/ASME Trans. Mechatronics*, vol. 30, no. 6, pp. 7762-7773, 2025.

[11] C. Zhou, *et al.,* "Ferromagnetic soft catheter robots for minimally invasive bioprinting, " *Nat. Commun.,* vol. 12, no. 1, 5072, 2021.

[12] J. Xia, *et al.*, "Learning-based real-time shape and force estimation for continuum robots using FBG-embedded actuation cables". In *IEEE/ASME Trans. Mechatronics,* doi: 10.1109/TMECH.2026.3659518.

[13] A. Gao, *et al.,* "Mechanical model of dexterous continuum manipulators with compliant joints and tendon/external force interactions, " *IEEE/ASME Trans. Mechatronics*, vol. 22, no. 1, pp. 465-475, 2016.

[14] Y. Fang, *et al.,* "Design and control of a multiple-section continuum robot with a hybrid sensing system," *IEEE/ASME Trans. Mechatronics,* vol. 28, no. 3, pp. 1522-1533, 2023.

[15] A. Gao, *et al.,* "Fiber Bragg grating-based triaxial force sensor with parallel flexure hinges," *IEEE Trans. Ind. Electron.,* vol. 65, no. 10, pp. 8215-8223, 2018.

[16] B. Mauzé, *et al.* "Nanometer precision with a planar parallel continuum robot, *IEEE Robot. Autom. Lett.,* vol. 5, no. 3, pp. 3806-3813, 2020.

[17] M. Abdelaziz, *et al.,* "Fiberbots: Robotic fibers for high-precision minimally invasive surgery,". *Sci. Adv.,* vol. 10, no. 3, eadj1984. 2024.

[18] L. Li, *et al.*, "Precise and high-load capacity miniature 6-DOF manipulator for microsurgery," *IEEE/ASME Trans. Mechatronics,* vol. 30, no. 3, pp. 1842-1852, 2024.

[19] B. Gil, *et al.,* "Miniaturized piezo force sensor for a medical catheter and implantable device, " *Appl. Electron. Mater.,* vol. 2, no. 8, pp. 2669-2677, 2020.

[20] C. Nwafor, *et al.*, "Miniature parallel continuum robot made of glass: Analysis, design, and proof-of-concept," *IEEE/ASME Trans. Mechatronics,* vol. 28, no. 4, pp. 2038-2046, 2023.

[21] C. Nwafor, *et al.,* "The Caturo: A submillimeter diameter glass concentric tube robot with high curvature," *Adv. Intell. Syst.,* vol. 5, no. 2, 2200308, 2023.

[22] A. Gao, *et al.,* "Laser-profiled continuum robot with integrated tension sensing for simultaneous shape and tip force estimation," *Soft Robot.,* vol. 7, no. 4, pp. 421-443, 2020.

[23] A. Gao, *et al.,* "Body contact estimation of continuum robots with tension-profile sensing of actuation fibers," *IEEE Trans. Robot.,* vol. 40, pp. 1492-1508, 2024.

[24] Z. Lin, *et al.,* "Real-time whole-body contact estimation of continuum robots using multiplexed fibers for embodied actuation and sensing to quantify interactions,". *Soft Robot.,* doi: 10.1177/2169517225138880.

[25] A. Gao, *et al.* "Modeling and task-oriented optimization of contact-aided continuum robots", *IEEE/ASME Trans. Mechatronics*, vol. 25, no. 3, pp:1444-1455, 2020.

[26] H. Suzuki, *et al.,* "Origami-inspired miniature manipulator for teleoperated microsurgery," *Nat. Mach. Intell.,* vol. 2, no. 8, pp. 437-446, 2020.

[27] Y. An, *et al.,* "A microscopic vision-based robotic system for floating electrode assembly," *IEEE/ASME Trans. Mechatronics*, vol. 29, no. 5, pp. 3810-3820, 2024.

[28] L. Scott, *et al*., "A low-cost teleoperable surgical robot with a macro-micro structure and a continuum tip for open-source research," *in Proc. IEEE Int. Conf. Adv. Intell. Mechatronics (AIM),* pp. 847-852, 2024.

[29] F. Cursi, *et al.,* "Optimization of surgical robotic instrument mounting in a macro–micro manipulator setup for improving task execution," *IEEE Trans. Robot.*, vol. 38, no. 5, pp. 2858-2874, 2022.

[30] E. Ahronovich, *et al.,* "Parallel mechanisms for multiscale motion msing twisted wire actuation: aesigning for microworkspace and dexterity." *ASME. J. Mechanisms Robotics,* vol. 17, no. 11, 111009, 2025.

[31] S. Zhang, *et al.,* "Piezo robotic hand for motion manipulation from micro to macro," *Nat. Commun.,* vol. 14, no. 1, 500, 2023.

[32] C. Zhou, *et al.,* "Submillimeter fiber robots capable of decoupled macro-micro motion for endoluminal manipulation," *Sci. Adv.,* vol. 10, no. 47, eadr6428, 2024.

[33] S. Ahmed, *et al.,* "Multi-scale motion of soft continuum robots using tendons, eccentric rods, and a cam, " *Proc. IEEE Int. Conf. Soft Robot. (RoboSoft),* pp. 184-190, 2021.

[34] L. Zeng, *et al.,* "Concentric-tube-eccentric-rod: a continuum actuator for macro-/micro-scale translational actuation," *in Proc. IEEE 20th Int. Conf. Autom. Sci. Eng. (CASE),* pp2052-2058, 2024.

[35] T. Vandebroek, *et al*., "Macro-micro multi-arm robot for single-port access surgery," *in Proc. IEEE/RSJ Int. Conf. Intell. Robots Syst. (IROS)*, pp. 425-432, 2019.

[36] A. Nazari, *et al*., "Visual servoing of continuum robots: Methods, challenges, and prospects," *Int. J. Med. Robot. Comput. Assist. Surg.,* vol. 18, no. 3, e2384, 2022.

[37] S. Russo, *et al*., "Soft pop-up mechanisms for micro surgical tools: Design and characterization of compliant millimeter-scale articulated structures," *in Proc. IEEE Int. Conf. Robot. Autom. (ICRA),* pp. 750-757, 2016.

[38] G. Del, *et al*., "Continuum robots for multi-scale motion: Micro-scale motion through equilibrium modulation," *in Proc. IEEE/RSJ Int. Conf. Intell. Robots Syst. (IROS)*, pp. 2537-2542, 2017.

[39] Z. Lin, *et al*., "Toward cable-driven continuum robots: Micro-motion augmentation using eccentrically arranged fibres with eccentric lumens," *in Proc. IEEE Int. Conf. Robot. Biomimetics (ROBIO)*, pp. 2160-2165, 2024.

[40] T. Wang, *et al.,* "A macro-micro vision integrated micromanipulation system for self-initialization and resilient control," *IEEE Trans. Autom. Sci. Eng.*, vol. 22, pp. 11250-11263, 2025.

[41] Y. Yin, *et al*., "Applications of uncalibrated image-based visual servoing in micro- and macroscale robotics," *in Proc. IEEE 19th Int. Conf. Autom. Sci. Eng. (CASE)*, pp. 1-8, 2023.

[42] R.J. Webster, *et al.,* "Design and kinematic modeling of constant curvature continuum robots: A review, ". *Int. J. Robot. Res.,* vol. 29, no. 13, pp. 1661-1683, 2010.

[43] A.A. Nazari, *et al.,* "Visual servoing of continuum robots: Methods, challenges, and prospects," *Int. J. Med. Robot. Comp.,* vol. 18, no. 3, e2384, 2022.

[44] Z. Li, *et al.,* "An end-to-end controller with image-based visual servoing of industrial manipulators with soft-actor-critic algorithm,". *Knowl. -Based Syst.,* vol. 311, 112980, 2025.